

Resveratrol-loaded PCL-PEG/GO/HAP biocomposite bone membranes: Evaluation of mechanical properties, release kinetics, and cellular response

Journal of Applied Biomaterials & Functional Materials
1–16
© The Author(s) 2025
Article reuse guidelines:
sagepub.com/journals-permissions
DOI: 10.1177/22808000251314087
journals.sagepub.com/home/jbf
 Sage

Betül Meryem Arpacay¹ , Fatih Ciftci^{1,2} , Ali Can Özarslan^{3,4} , Mustafa Unal^{5,6} , Mine Kucak⁷ and Aslihan Yelkenci⁸

Abstract

In this study, biocomposite membranes were developed by incorporating resveratrol (RSV)-loaded PCL-PEG composites, modified with graphene oxide (GO) and hydroxyapatite (HAP). The aim was to enhance hydrophilicity with GO and improve bioactivity with HAP. The release kinetics of RSV was evaluated by using Franz diffusion cells and compared with various kinetic models, including Korsmeyer-Peppas, Higuchi, and Baker, all of which showed high correlation coefficients (R^2) close to 0.99. Mechanical tests were performed to determine the suitability of these membranes for tissue engineering applications. The composite membrane modified with GO and HAP exhibited tensile strength of 105.2 ± 5.8 MPa, tensile modulus of 3895 ± 159 MPa, elongation at break of $8.4 \pm 0.9\%$, and toughness of 5.88 ± 0.46 MJ/m³. In vitro cell adhesion studies, visualized using DAPI fluorescence staining, demonstrated increased cell adhesion to the composite membranes over periods of 1, 3, 5, 7, and 14 days. These findings highlight the potential of the RSV-loaded PCL-PEG membranes, enhanced with GO and HAP, for applications in bone tissue engineering.

Keywords

Bone tissue engineering, polymer-matrix composites, drug releasing, release kinetics, biocomposite membrane

Date received: 23 September 2024; revised: 10 December 2024; accepted: 2 January 2025

¹Department of Biomedical Engineering, Fatih Sultan Mehmet Vakıf University, Istanbul, Turkey

²Department of Technology Transfer Office, Fatih Sultan Mehmet Vakıf University, Istanbul, Turkey

³Faculty of Engineering, Department of Metallurgical and Materials Engineering, Istanbul University-Cerrahpasa, Istanbul, Turkey

⁴Health Biotechnology Joint Research and Application Center of Excellence, Istanbul, Turkey

⁵Department of Orthopedic Surgery, Harvard Medical School, Boston, MA, USA

⁶Center for Advanced Orthopedics Studies, Beth Israel Deaconess Medical Center, Boston, MA, USA

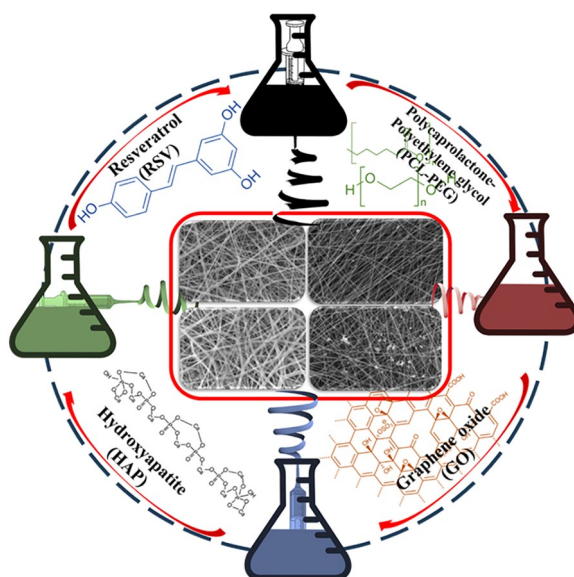
⁷Department of Molecular Biology and Genetics, Yıldız Technical University, Istanbul, Turkey

⁸Faculty of Dentistry, Department of Pediatric Dentistry, University of Health Sciences, Istanbul, Turkey

Corresponding author:

Fatih Ciftci, Department of Biomedical Engineering, Fatih Sultan Mehmet Vakıf University, Merkez Efendi Mah. Mevlevihane Cad. Yenikapı Mevlevihanesi No: 25 Teknoloji Transfer Ofisi, Zeytinburnu, Istanbul 34349, Turkey.
Emails: fciftci@fsm.edu.tr; faciftcii@gmail.com





Graphical abstract of resveratrol (RSV) loaded PCL-PEG, PCL-PEG-Graphene oxide (GO), PCL-PEG-Hydroxyapatite (HAP) and PCL-PEG-HAP-GO biocomposite membrane produced by electrospinning method.

Introduction

Bone tissue engineering (BTE) has gained significant attention in recent years due to the increasing prevalence of bone-related disorders¹ and the limitations of current treatment options. BTE has emerged as a transformative approach to addressing complex challenges in the repair and regeneration of damaged bone tissue. The traditional methods for bone repair, including autografts, allografts, and synthetic bone substitutes, have constituted a pivotal aspect of clinical practice.² Autografts, which involve the harvesting of bone from the patient's own body, are regarded as the gold standard due to their biological compatibility and osteogenic potential. However, these approaches are limited by donor site morbidity, surgical complexity, and the limited availability of donor bone.³ Allografts, derived from cadaveric donors, do not require a second surgical site but are associated with risks of immune rejection, disease transmission, and variable incorporation into the host bone.³ Synthetic bone substitutes, such as calcium phosphate ceramics and bioactive glasses, provide a convenient and reproducible alternative but often lack the biological stimuli necessary for optimal bone regeneration.⁴ These traditional approaches, while demonstrating efficacy to varying degrees, are constrained by significant limitations. The major challenges encompass the necessity for optimized drug delivery systems to facilitate bone healing, the development of scaffolds with tailored mechanical and biological properties, and the provision of sustained release of therapeutic agents to enhance regenerative outcomes. Consequently, there is an unmet need for advanced materials that can address these limitations and promote more effective bone regeneration.

The development of scaffolds that are capable of effectively supporting bone regeneration is of great importance for the successful implementation of BTE applications. Among the numerous materials that have been explored, polycaprolactone (PCL), polyethylene glycol (PEG), graphene oxide (GO), and hydroxyapatite (HAP) have demonstrated particular promise as candidates for the creation of biocomposite membranes that can enhance the mechanical and biological properties of scaffolds.^{5,6} PCL is a biodegradable polyester that exhibits excellent mechanical properties rendering it a suitable candidate for bone tissue engineering applications. Its slow degradation rate allows for sustained support during the healing process, which is essential for large bone defects.⁷ The integration of PEG into PCL scaffolds can enhance hydrophilicity and facilitate cell adhesion and proliferation, which are pivotal for efficacious bone regeneration.⁸ The incorporation of PCL and PEG has been demonstrated to generate a conducive microenvironment for osteoblasts, stimulating their growth and differentiation.⁹

GO has also attracted considerable interest in the field of BTE due to its distinctive properties, including a high surface area, mechanical strength, and biocompatibility. Moreover, GO has been demonstrated to enhance the osteogenic potential of scaffolds by providing a conducive environment for cell attachment and proliferation¹⁰ GO can also enhance the mechanical properties of PCL scaffolds, rendering them more suitable for load-bearing applications.⁷ The release of GO is beneficial for cells in some biomedical applications but may lead to toxicity in the absence of a controlled release mechanism. In addition, the release of GO at high concentrations may inhibit proliferation and trigger apoptosis in cells. This is particularly important for bone

cells (osteoblasts) and cartilage cells (chondroblasts).^{11,12} Moreover, the integration of GO into PCL/PEG scaffolds has been demonstrated to enhance the release of bioactive molecules, which can further stimulate osteogenic differentiation.¹³ HAP, a naturally occurring mineral form of calcium apatite, is also a crucial component in bone tissue engineering because of its structural and compositional similarity to bone mineral. HAP has the capacity to enhance the bioactivity of scaffolds, thereby promoting mineralization and integration with surrounding bone tissue.¹⁴ Although HAP is considered an ideal material for bone regeneration, its excessive release during scaffold degradation can disrupt the balance of calcium and phosphate in the surrounding tissues, leading to mineral deposits (e.g., calcification). HAP particles can trigger an inflammatory response in surrounding tissues. This can impair tissue integrity and negatively affect the healing process.¹⁵⁻¹⁷

The combination of HAP with PCL and GO has been demonstrated to yield a composite scaffold that not only mimics the mechanical properties of bone but also facilitates osteoconductivity and osteoinductivity.¹⁸ The incorporation of HAP into the scaffold markedly enhances calcium deposition, which is a vital process in bone regeneration.⁹ Recent advances in the fabrication techniques for these biocomposite membranes, including electrospinning and 3D printing, have enabled the creation of scaffolds with tailored architectures and porosities that mimic the natural bone structure.^{19,20} The incorporation of hierarchical structures within the scaffolds can further enhance their mechanical properties and biological performance.²¹

Resveratrol (RSV), a natural polyphenolic compound, has been shown to possess significant osteogenic properties. Moon et al.²² demonstrated that RSV can enhance mitochondrial biogenesis and osteogenic differentiation in human periosteum-derived MSCs, suggesting its potential as a therapeutic agent in BTE. Similarly, Wajima et al.²³ reported that RSV treatment improved bone density and healing in type 2 diabetic rats, indicating its role in modulating osteogenic and osteoclastogenic mechanisms during bone remodeling. Moreover, Ozturk et al.²⁴ reported that RSV showed the preventive effects on bone quality deterioration caused by ovariectomy-induced osteoporosis in rats. Bo et al.,²⁵ found that RSV supplementation positively affected bone health in type 2 diabetic patients, indicating its potential as an anabolic agent for enhancing bone density. These findings cumulatively suggest that incorporating RSV into scaffolds could provide additional benefits in promoting bone regeneration, particularly in patients with metabolic disorders. In addition to mechanical and biological enhancements, the use of RSV-loaded biocomposite membranes may also address challenges related to inflammation and oxidative stress in the bone healing process. RSV has also gained attention for its antioxidant and anti-inflammatory properties.²⁶ For instance, RSV has been shown to exert antioxidant effects, which can mitigate oxidative stress and inflammation, common issues in

diabetic patients and those with compromised bone healing.²⁷ This property could further enhance the healing environment provided by the scaffolds, promoting better integration with host tissues. Although RSV is known for its antioxidant and anti-inflammatory properties, some problems can arise when it is released in large quantities from the scaffold. For example, sustained high doses of RSV may lead to unwanted stimulation or inhibition of cells surrounding the skeleton, potentially affecting the balance of cellular activities and interfering with bone regeneration processes.^{28,29} Therefore, the controlled release of RSV from the scaffold can provide a sustained therapeutic effect, further supporting bone regeneration. One of the primary challenges in incorporating RSV into scaffolds is achieving controlled and sustained release of the compound to maximize its therapeutic efficacy. Electrospinning has emerged as a versatile technique for fabricating nanofibrous membranes that offer high surface areas and controlled drug release properties.^{30,31} This method allows for the creation of scaffolds with precise control over fiber diameter and morphology, which are critical for drug delivery and tissue integration.³²

The development of RSV-loaded PCL-PEG/GO/HAP biocomposite membranes may represent a new promising approach in BTE. Accordingly, this study aimed to develop and characterize RSV-loaded biocomposite membranes using PCL-PEG, GO, and HAP for BTE applications. Towards that end, the primary objectives of this research were to evaluate the *in vitro* release kinetics of RSV from these biocomposite membranes and to assess their impact on cell performance.

Materials and methods

Polycaprolactone (PCL, Mw=80.000 g/mol), PEG (Mw=2000) and Resveratrol (RSV) were purchased from Sigma-Aldrich (Munich, Germany). Dichloromethane (DCM) was purchased from Merck (Darmstadt, Germany). All materials are chemically stable and biocompatible. Sulfuric acid (H₂SO₄), potassium permanganate (KMnO₄), phosphoric acid (H₃PO₄) and hydrogen peroxide (H₂O₂) were purchased from Sigma-Aldrich to synthesis of Graphene oxide. Calcium nitrate tetra-hydrate (Ca(NO₃)₂·4H₂O), ammonium di-hydrogen phosphate ((NH₄)H₂PO₄) and ammonia solution (NH₄OH) were supplied from Sigma-Aldrich/Germany to synthesis of Hydroxyapatite (HAP) and sodium tripolyphosphate (Sigma-Aldrich/Germany) was selected as the surfactant.

Synthesis of hydroxyapatite nano-powder

HAP nano-powder were synthesized via wet chemical precipitation method using previously described by Ozder et al.³³ HAP precipitate and water were formed by the reaction of acid and alkaline solutions (ammonium di-hydrogen phosphate and calcium nitrate tetra-hydrate,

respectively) which were used to synthesize HAP nanopowder as precursors. The experimental temperature was set to 25°C and the pH of reaction medium was set to above 10 to achieve desired features of HAP. Briefly, 0.1 mole of calcium nitrate tetra-hydrate and 0.02 mole ammonium di-hydrogen phosphate were separately dissolved in 100 mL distilled water. Then, pH of the two solutions was adjusted by ammonium solution by 10 and ultrasonicated for 10 min. When these two solutions were dropped into one another, HAP nanopowder formed as a precipitate. The precipitated HAP nanopowder was washed with distilled water and centrifuged at 4100 rpm for 4 min and this process was repeated six times.

Synthesis of graphene oxide

Initially, a 1 L beaker was prepared, and into it, a mixture of 360 mL concentrated sulfuric acid and 40 mL phosphoric acid was added. To facilitate thorough mixing, a large stir bar was introduced, and the beaker was positioned in an oil bath, ensuring that the oil level surpassed the liquid level within the beaker. The oil bath was set to maintain a temperature of 60°C, while a thermometer was inserted into the synthesis volume to monitor and control the temperature. Simultaneously, the stir plate was adjusted to a stirring speed of 200 rpm. Subsequently, a gradual addition of 3.0 g graphite and 18.0 g potassium permanganate was carried out within the acid mixture and the reaction mixture was carefully poured into the ice-filled beaker. Additionally, 3–5 aliquots of 3 mL of 30 wt.% hydrogen peroxide were introduced. This induced a transition in the suspension from a purple hue to a vibrant yellow coloration with discernible bright white specks. To further purify the resultant product, it underwent a thorough washing process consisting of six successive rinses with distilled water, followed by centrifugation at 3000 rpm for a duration of 45 min. The acid component was subsequently disposed down the drain, accompanied by a copious amount of running water. The product was further subjected to washing with pure water, wherein each centrifuge tube was filled with pure water and a glass rod was utilized to disrupt the pellet. Once again, centrifugation was conducted at 3000 rpm for 45 min. This washing procedure was repeated three times, this time utilizing 35 wt.% concentrated hydrochloric acid. The pellet was gently disrupted using a glass stir rod, and the tubes were gently agitated to promote better mixing. Centrifugation was then repeated at 3000 rpm for 45 min. Following this, the product was washed three times with anhydrous ethanol and subjected to centrifugation at 3000 rpm for 45 min, yielding graphene oxide in an ethanol solution (GO).

Preparation of biocomposite nanofibers

PCL was dissolved with various percentages as 1, 3, 5, and 7 wt.% in Dichloromethane (DCM) was stirred with the

magnetic stirrer at room temperature (23°C) for 1 h. After that step 0.005 g PEG and RSV were added separately in 3 wt.% PCL solution and mixed with magnetic stirrer for 1 h.

The GO and HAP materials were fully dissolved using three cycles of ultrasonication lasting for 2 h each, followed by 30 min of stirring to create dispersions. Cold water was periodically added to the ultrasonic bath to maintain a constant temperature. Next, the GO and HAP dispersions, each at a concentration of 1 wt.%, were mixed with 10% PCL-PEG in continuous magnetic stirring overnight at room temperature. A 10% PCL solution was selected due to its ideal properties for Electrospun materials.

A conventional Electrospun equipment (Inovenso Co., Istanbul, Fatih Sultan Mehmet Vakif University, BIORGINE Lab, Turkey) was used to prepare pure PCL-PEG, PCL-PEG-RSV, PCL-PEG/GO, PCL-PEG/GO-RSV and PCL-PEG/GO/HAP/RSV composites. The mixture was introduced into a 10 mL glass syringe equipped with a 19-gauge stainless steel needle and subsequently subjected to the electrospinning process under constant conditions.

The selection of the electrospinning process parameters such as flow rate, needle-to-collector distance, voltage, temperature, and humidity are critical for controlling the morphology and properties of the resulting biocomposite fibers.³⁴ The parameters used were as follows: a flow rate of 1 mL/h, a needle-to-collector distance of 15 cm, a high voltage of 15 kV, and a controlled temperature of 25°C with a relative humidity of 40%. The resulting fibers were collected on an aluminum foil-covered, grounded rotary drum with a diameter of 100 mm. The drum rotated at a speed of 5 rpm, and the collection process lasted for 90 min. After collection, the biocomposite membranes were carefully dried for a minimum of 2 days under a fume hood to effectively eliminate any residual solvents.³¹ The prepared biocomposite membrane (BCM) groups were named PCL-PEG, PCL-PEG-RSV; BCM1, PCL-PEG/GO; BCM2, PCL-PEG/GO-RSV; BCM3 and PCL-PEG/GO/HAP/RSV; BMC4.

Characterization

Morphological analysis

The morphological characteristics of the biocomposite membranes were examined using scanning electron microscopy (SEM) with an EVO LS 10 (ZEISS) microscope. The SEM was operated at an accelerating voltage of 5 kV (5 KX magnification) in secondary electron mode to capture high-resolution images of the membrane surface. To overcome the non-conductive nature of the polymer samples, all BCM specimens were sputter-coated with a thin layer of gold-palladium alloy to ensure adequate conductivity and image clarity. Fiber diameter distribution was quantitatively assessed using the Diameter J plugin for ImageJ software, which enables automated analysis of fiber diameters from SEM images. Diameter J processes

the images by evaluating the diameter of nanofibers at each pixel along the fiber axis, generating a histogram to represent the diameter distribution. The tool also provides summary statistics, including the mean fiber diameter, offering a comprehensive characterization of the membrane's morphological features.

Transmission electron microscopy (TEM) was employed to analyse the morphology of the synthesized GO. For this analysis (Hitachi HF-2000 TEM), 10 mg of GO powder was dispersed in 20 mL of ethanol. The suspension was then dropped onto carbon-coated copper grids and allowed to air-dry for 10 min. The prepared grid was subsequently positioned in the instrument chamber, and imaging was conducted at an accelerating voltage of 200 kV.

FTIR analysis

Fourier Transform Infrared Spectroscopy (FTIR) was performed using a Shimadzu spectrometer to identify the functional groups present in the biocomposite membranes. The analysis was conducted in the wavenumber range of 4000–400 cm^{-1} , providing a comprehensive assessment of the molecular vibrations corresponding to various functional groups.³⁵ The samples were prepared and mounted appropriately to ensure optimal signal acquisition. The resulting spectra were collected and analyzed to determine the characteristic peaks, which were subsequently assigned to specific functional groups present within the biocomposite membranes.

XRD analysis

X-ray diffraction (XRD) analysis was conducted using a Panalytical XPERT-PRO diffractometer to determine the crystal structure of the biocomposite membranes. The measurements were performed using a Cu $K\alpha$ radiation source, with an internal wavelength of 1.54 Å, powered by a 40 mA current and a 45 kV voltage generator.³⁶ The XRD patterns were recorded over a 2θ range from 10° to 70°, providing detailed information on the crystallographic phases and degree of crystallinity within the biocomposite membranes. The collected diffraction data were analyzed to identify and quantify the crystalline phases present in the samples.

Mechanical analysis

The mechanical properties of the BCM and PCL-PEG material were evaluated using a tensile mechanical test, following the standard procedure outlined in ASTM D882.³⁷ The samples were processed into rectangular strips with dimensions of 100 mm \times 20 mm \times 0.1 mm. The test was conducted using a universal testing machine, where the samples were subjected to a uniaxial tensile load

at a constant crosshead speed of 5 mm/min until the fracture point was reached. The force and elongation were recorded throughout the test to calculate the tensile strength, elongation at break, toughness and Young's modulus of the tested materials. Toughness was calculated as the energy absorbed by the BCM samples before the fracture by the area under the stress-strain curve.

Encapsulation efficiency and RSV loading efficiency

The experiment was designed to assess the release profile and loading efficiency of BCM samples loaded with RSV. The BCM samples were immersed in a phosphate-buffered saline (PBS) solution at pH 7.4, maintained at a concentration of 1 mg/mL. The RSV-loaded samples in the PBS solution were subjected to centrifugation at predetermined time intervals (15, 30, 45, 60, 120, 240, 300, 360, 420, and 480 min) for a total duration of 8 h.³⁸ After each centrifugation period, the process was halted, and the supernatant was carefully collected for further analysis. The UV absorption spectra of the collected supernatants were measured using a UV-visible spectrophotometer (UV-1280, SHIMADZU, Japan) to determine the concentration of RSV released into the PBS. Fresh PBS was used for each experiment to maintain consistent conditions throughout. The encapsulation efficiency (EE) and RSV loading efficiency (LE) were calculated using standard formulas to quantify the amount of RSV encapsulated within the PCL-PEG polymeric composites. The RSV loading in the composites was determined using equation (1), which relates the mass of RSV loaded to the total mass of the composite.

$$EE\% = \frac{(\text{Total Active Added} - \text{Free Active})}{\text{Total Active Added}} \times 100 \quad (1)$$

For determining loading efficiency, dried samples weight measured and loading efficiency were determined according to equation (2).

$$LE\% = \frac{\text{Active Ingredient in Capsules}}{\text{Total Weight of Dried Microcapsules}} \times 100 \quad (2)$$

In vitro studies release kinetics model

Release studies were performed with slight modifications of a procedure described in literature.^{39–41} Briefly, 10 mg of samples added into 50 mL of release media consisting of dH_2O and EtOH in 3:2 volumetric ratio. Suspension mixed with a magnetic stirrer at 500 rpm, 1 mL of samples were taken hourly within the first 8 h and 24th h. Taken samples

were centrifuged for 10 min at 9000 rpm and supernatants were analyzed at the proper wavelengths with Epoch II Multiplate Reader (Biotek Instruments). Released amount of active ingredients were determined with calibration curve calculations and cumulative release percentage was calculated depending on equation (3).

$$\text{Cumulative Release \%} = \frac{\text{Released Active Ingredient}}{\text{Loaded Active Ingredient}} \times 100 \quad (3)$$

The release of RSV from the prepared biocomposite membranes were studied using Franz diffusion cells. The Franz diffusion device is a commonly used in vitro technique for measuring dermal absorption, where the active ingredient is applied to the surface of a skin sample. In the case of biocomposite samples, the most common method for dissolution testing involves using the Franz diffusion device.²⁶ In this study, the composites containing the active substance were placed in the membrane section of the Franz device. The experiment was conducted at a constant ambient temperature of 37°C with continuous mixing. At specific time points (15th and 30th min, 1st, 2nd, 4th, 6th, 8th, and 24th h), 2.5 mL of the sample was collected from the lower part of the diffusion cell and replaced with fresh medium preheated to 37°C. This process was repeated throughout the experiment. The collected samples were then analyzed using high-performance liquid chromatography (HPLC) to determine the amount of active substance present. The cumulative percentage of the active substance passing through the cells was plotted against time, and the cumulative percentage passed at the end of 24 h was calculated. Statistical analysis of the cumulative mass losses for the biocomposite membranes were performed using the Minitab program. The encapsulation efficiency and RSV loading were calculated using equations (1) and (2). The release kinetics of the RSV drug loaded into the BCM samples were analyzed by using different models; zero-order, first-order, Higuchi, Hixson, Korsmeyer–Peppas, and Baker mathematical model. The effectiveness of various release profiles was evaluated using the correlation coefficient (R^2). It was determined that the mathematical model showing the highest correlation coefficient was the most appropriate representation of drug release kinetics.²⁶

Evaluation of cell line and adhesion

The BCM samples were subjected to sterilization before being cultured in DMEM, which served as the cellular nutrition source, resembling ECM. NIH 3T3 mouse embryonic fibroblast cells were utilized for the experiments and were cultured after isolation from a cell line. Each BCM sample was seeded with approximately 7×10^4 NIH-3T3 cell lines. After 72 h of cell culture, the cells

were stained with DAPI (5 mM) dyes and subsequently examined using fluorescence microscopy to visualize their characteristics and behaviors.

Statistical analysis

The results were expressed as the mean \pm standard deviation (SD) and were derived from three independent assays, each performed in triplicate to ensure reliability and reproducibility. Statistical analysis was conducted using one-way analysis of variance (ANOVA) to assess the significance of differences between groups. A p -value of less than 0.05 was considered to indicate statistical significance, ensuring that any observed differences were unlikely due to random variation. Post hoc analysis was performed, where applicable, to further evaluate pairwise comparisons between groups.

Result

Morphological analysis

As shown in Figure 1, SEM analysis demonstrated the successful fabrication of all the samples. The fiber diameter of the PCL-PEG composite was measured at 432.439 ± 150.946 nm (Figure 1(a)). The diameter of the BCM1 composite fibers, incorporating RSV into the PCL-PEG structure, was recorded as 466.64 ± 284.082 nm (Figure 1(b)). Comparison of the PCL-PEG and BCM1 composites indicated that the fiber diameter expanded upon drug loading. The HAP-incorporated PCL-PEG-RSV (BCM2) composite fibers exhibited a diameter of 623.74 ± 158.099 nm, attributed to the crystal structure and surface area of HAP (Figure 1(c)). In addition, the diameter of GO-incorporated PCL-PEG-RSV composite fibers was observed to be 517.85 ± 163.523 nm (Figure 1(d)). Further, the fiber diameter of the GO-HAP-coincorporated PCL-PEG-RSV composite was observed at 1386.055 ± 355.193 nm (Figure 1(e)). A TEM image of GO (Figure 1(f)) showed that the samples possessed multiple layers due to their powdered form, with GO displaying an irregular shape, thick flat flake layers, a rough surface, non-wrinkled structure, and non-uniform particle size. Overall, the significant enlargement in fiber size of the drug-loaded PCL-PEG composite was attributed to the critical structure of HAP and the surface-wide architecture of GO.

FTIR and XRD

FTIR spectra revealed distinctive peaks of various samples, including standard compounds, physical mixtures, and BCM materials (Figure 2(a)). Significant changes in the peaks were detected in the spectra of composite materials with and without RSV, indicating notable differences in their composition. In the FTIR spectra, the characteristic

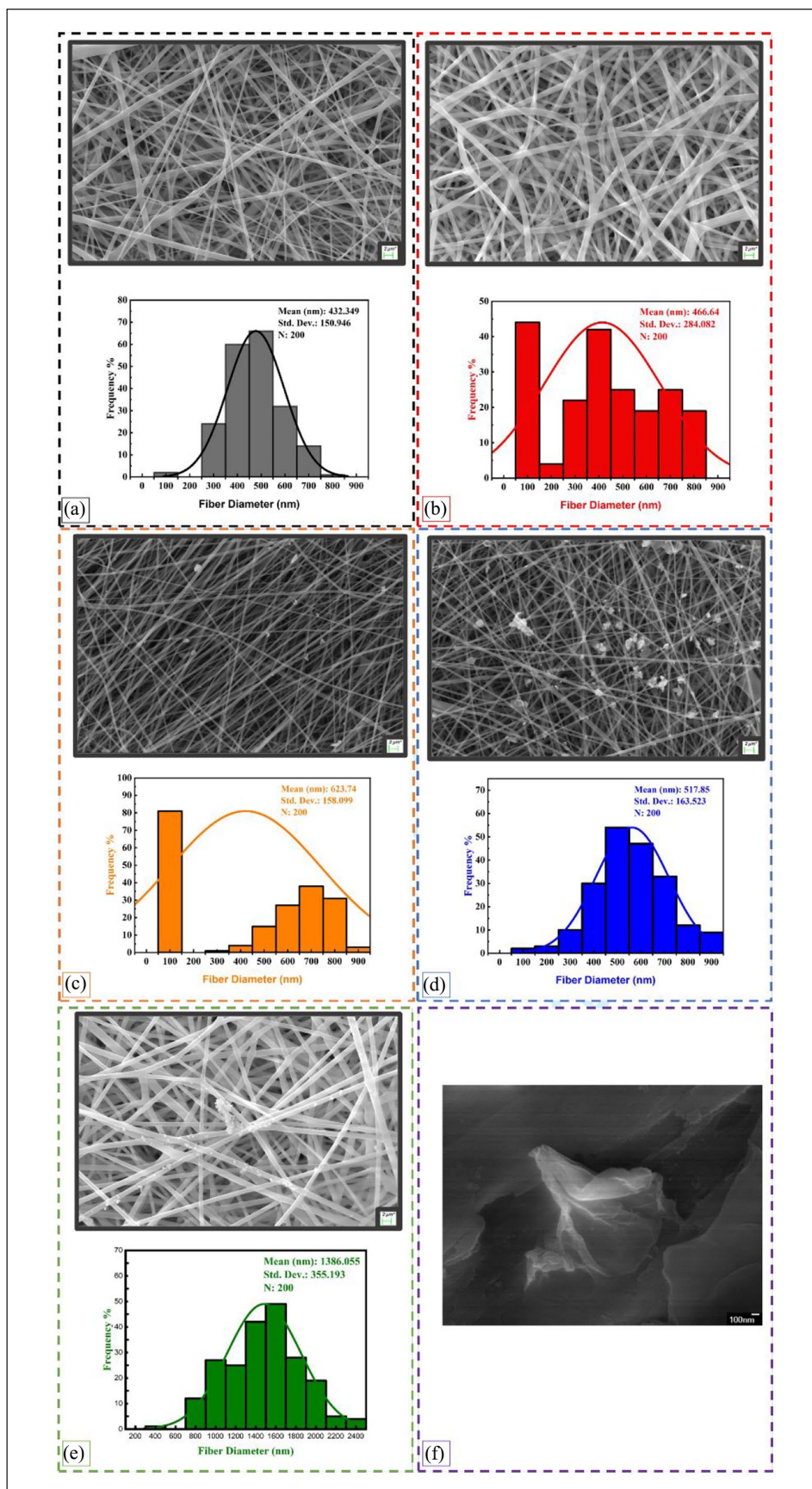


Figure 1. SEM images (5KX magnification) of (a) PCL-PEG, (b) BCM1, (c) BCM2, (d) BMC3, (e) BMC4, and TEM image of (f) GO.

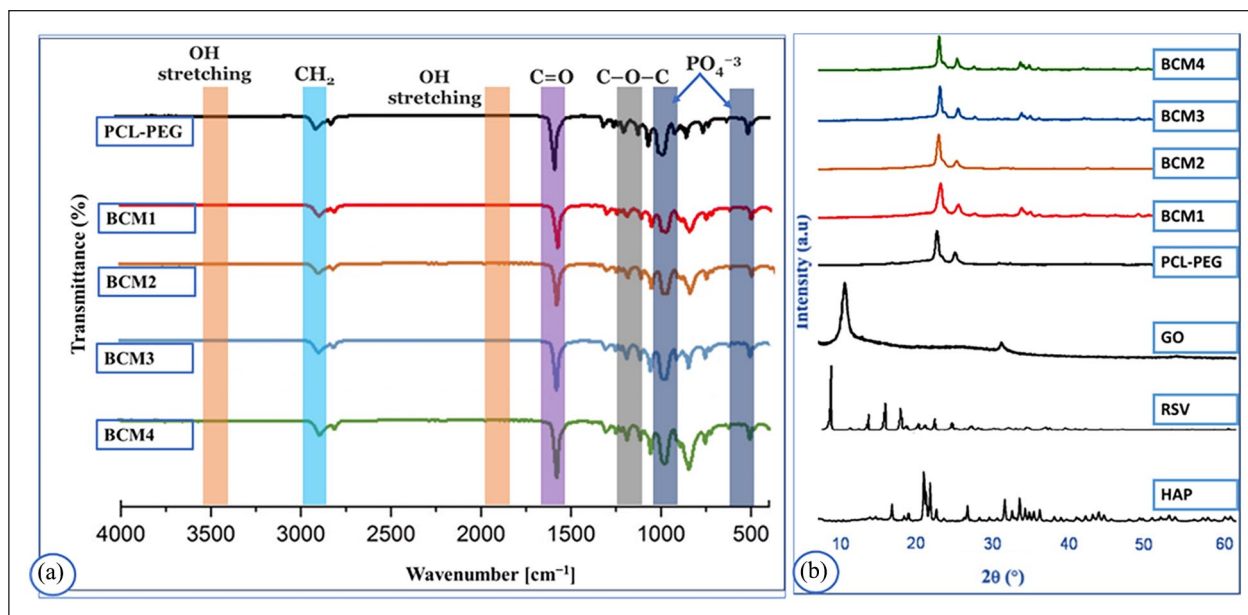


Figure 2. (a) FTIR spectra of the samples and (b) XRD patterns of the samples.

peak corresponding to the -OH stretching of PCL was identified at 3442 cm^{-1} . An additional peak at 1732 cm^{-1} indicated the presence of the aliphatic ester group in PCL. Furthermore, bands at 2858 and 2923 cm^{-1} were observed, corresponding to the CH_2 stretching of PCL. Characteristic peaks for PEG were found in the following vibrational regions. The bands at 2942.9 and 2849.5 cm^{-1} were related to the symmetric and asymmetric stretching of CH_2 groups, respectively. An intense vibration band related to the carbonyl group $\text{C}=\text{O}$ was confirmed at 1720 cm^{-1} . In addition, the asymmetric and symmetric $\text{C}-\text{O}-\text{C}$ stretching vibrations were shown at 1240 and 1169 cm^{-1} . The peak at 3431 cm^{-1} exhibited characteristic bands for the phenolic -OH group, the band at 897.1 cm^{-1} is attributed to C-H bending vibration.^{33,42} The same bands were observed for HAP, PCL-PEG in BCM3 and BCM4 structure. In BCM3 and BCM4 composites, the bands at 1028 and 983 cm^{-1} assigned to PO_4^{3-} deformation confirm the presence of HAP. The spectra of BCM2 and BCM4 composites were observed to have a broad and intense absorption band in the region $3600\text{--}2400\text{ cm}^{-1}$ corresponding to some OH stretching vibration and two recognizable absorption bands at 1723 and 1619 cm^{-1} .^{43,44}

As shown in Figure 2(b), BCM composite structures had their own characteristic pattern. For the PCL-PEG structure, peaks at 20.8° and 22.5° were observed in the (111) and (200) planes. When HAP was added to the PCL-PEG structures, the XRD curves of the BCM3 and BCM4 composites confirmed the presence of hydroxyapatite due to the presence of new peaks at 2θ of 32° and 33° referring to the (211) and (300) planes, respectively. The presence of GO structures was confirmed by the peak observed at 12° in the (002) plane. This peak was not detectable in the

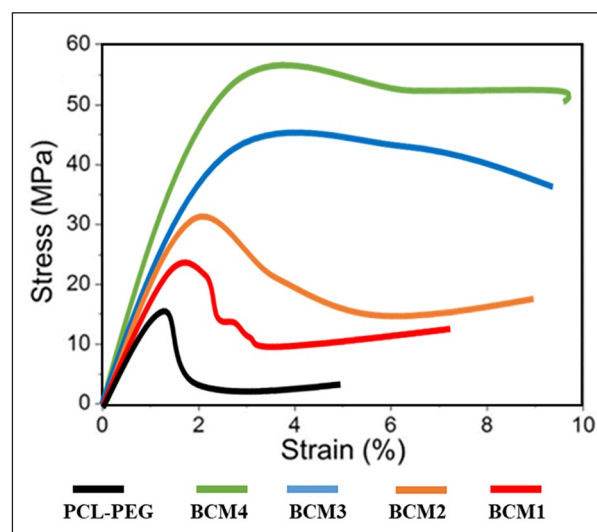


Figure 3. Stress-strain curves of samples.

composite materials due to the low amount of GO loaded in the BCM2 and BCM4 structures.^{26,45–48}

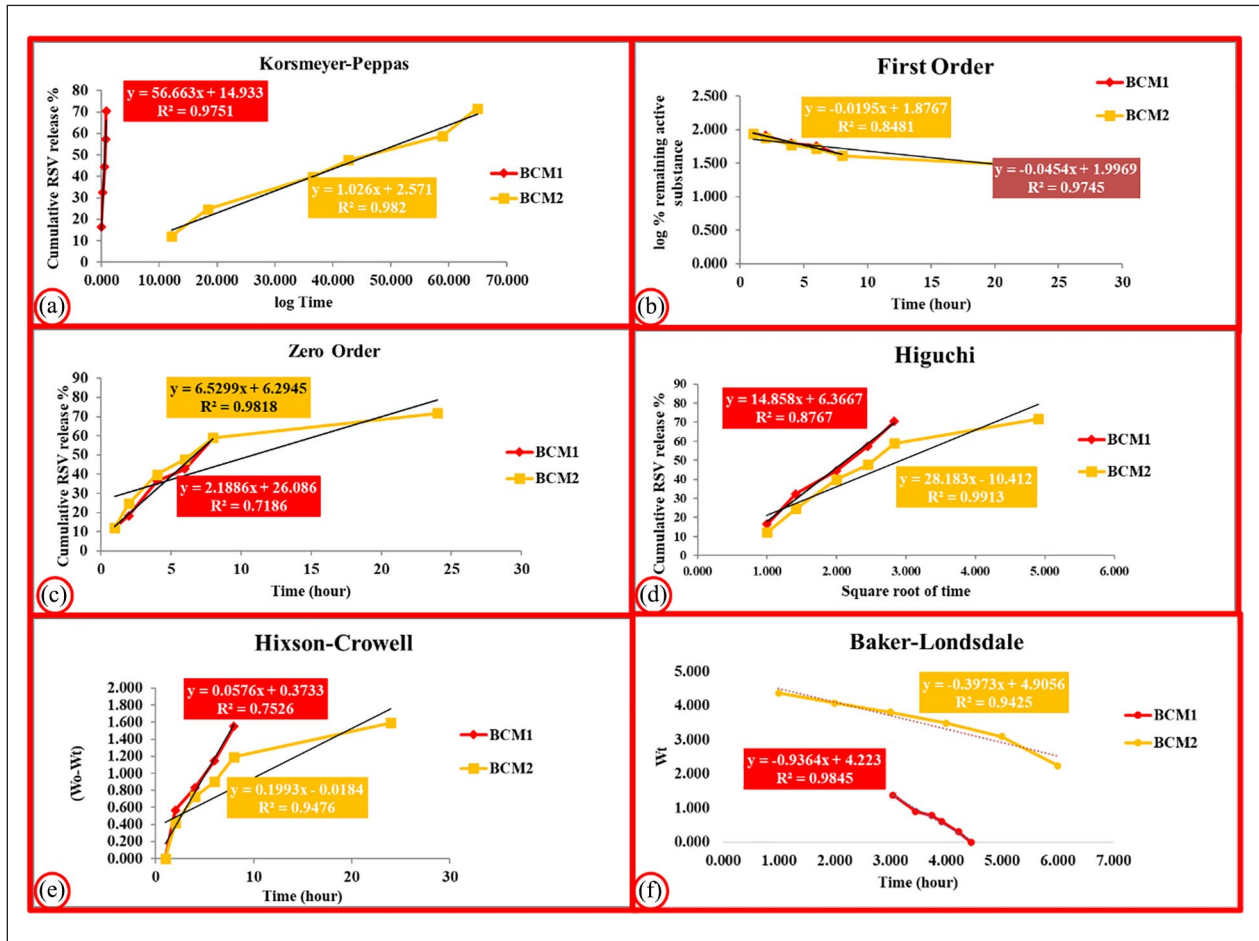
Mechanical properties

The stress-strain plot of materials (Figure 3) provided valuable insights into the mechanical properties of the PCL-PEG and BCM's. The composites fractured directly from the yield point with an elongation of PCL-PEG; 4.9% , BCM1; 7.2% , BCM2; 9.0% , BCM3; 9.3% , and BCM4; 9.8% , respectively.

As shown in Table 1, the detailed values of the mechanical properties were obtained from the stress-strain curves

Table 1. Tensile properties of samples.

Composite samples	Tensile strength (MPa)	Tensile modulus (MPa)	Elongation at break (%)	Toughness (MJ/m ²)
PCL-PEG	39.6 ± 3.9	2293 ± 142	5.0 ± 0.4	1.59 ± 0.15
BCM1	30.5 ± 2.3	2973 ± 116	2.8 ± 0.3	0.66 ± 0.09
BCM2	45.3 ± 3.1	2276 ± 135	5.6 ± 0.6	1.99 ± 0.23
BCM3	93.2 ± 4.9	3513 ± 182	7.4 ± 0.8	5.06 ± 0.30
BCM4	105.2 ± 5.8	3895 ± 159	8.4 ± 0.9	5.88 ± 0.46

**Figure 4.** Release kinetics of RSV active substance contents in BCM1 and BCM2 via Franz Diffusion mathematical models; (a) Korsmeyer–Peppas, (b) first Order model, (c) zero order, (d) Higuchi, (e) Hixson–Crowell, and (f) Baker–Lonsdale.

for PCL-PEG and BCM materials. A gradual increase in toughness was observed from sample BCM1 to sample BCM4, corresponding directly to the increasing incorporation of GO, RSV, and HAP materials into the PCL-PEG composites.^{45,49}

In vitro release study

In vitro release kinetic curves of BCM1, BCM2, BCM3, and BCM4 were shown in Figures 4 and 5. The results of the release kinetic analysis showed that the release model of correlation coefficient (R^2) values was 0.9845

(Baker-Lonsdale mathematical model) (Figure 4(f)), 0.9913 (Higuchi mathematical model) (Figure 4(d)), 0.9725 (Baker-Lonsdale mathematical model) (Figure 5(f)), and 0.9773 (Korsmeyer–Peppas mathematical model) for BCM1, BCM2, BCM3, and BCM4, respectively. As a result, it was determined that the release profile of RSV drug was concentration dependent. To understand the drug release mechanism, the release data were analyzed using the Baker–Lonsdale, Higuchi and Korsmeyer–Peppas equations, which give an idea about the diffusion type, respectively.^{26,50–53} The corresponding graph generated through the mathematical model equations exhibited a high

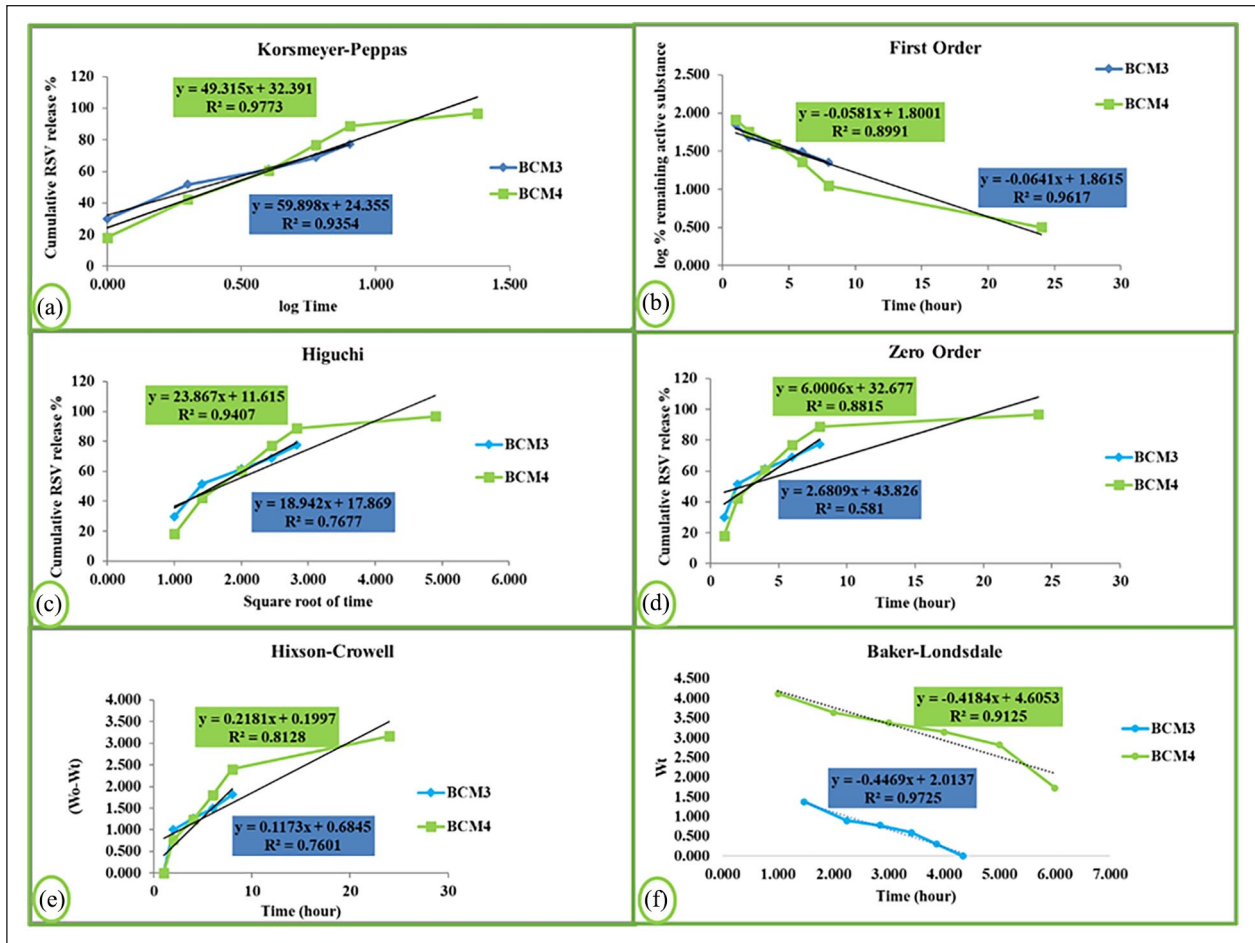


Figure 5. Release kinetics of RSV active substance contents in BCM3 and BCM4 via Franz Diffusion mathematical models; (a) Korsmeyer–Peppas, (b) first order model, (c) zero order, (d) Higuchi, (e) Hixson–Crowell, and (f) Baker–Lonsdale.

degree of linearity. As shown by the correlation coefficient greater than or equal to 0.90, this value indicated that the super state release into three different models. The release profile showed a combination of diffusion controlled and swelling controlled RSV release.

Cell line

The evaluation of cell attachment and proliferation on the BCM constructs was achieved through DAPI fluorescence imaging of live cells on the BCM samples after 1, 3, 5, 7, and 14 days of incubation (Figure 6). The obtained fluorescence images revealed noteworthy observations. Cells cultured on the surface of BCM2 and BCM4 samples (Figure 6) displayed a notably higher affinity for the PCL-PEG component when compared to both the control group and BCM1 samples.

Significant increases in cell numbers were observed on all BCM samples tested compared to the PCL-PEG control group (* in Figure 7, $p < 0.05$) (Figures 6 and 7). The highest observed cell numbers were observed on BCM3 and BCM4 samples at day 7 and 14 ($p < 0.05$) (Figures 6 and

7), which were statistically similar. It was observed that all samples did not negatively affect the cells and allowed cell attachment and proliferation during the in vitro test period.

Discussion

The ultimate goal of this study was to enhance the mechanical, biological, and drug delivery characteristics of the scaffolds to optimize bone tissue engineering. Towards that end, RSV-loaded PCL-PEG membranes were developed by incorporating with GO and HAP. Especially, the simultaneous release of GO, RSV and HAP and their interaction with each other can cause potential problems. For example, the propensity of GO to generate ROS may conflict with the antioxidant properties of RSV. This can lead to a complex mechanism of action in the cellular environment and can have both positive and negative consequences on the cells. As these three components have different bioavailability times, the prolonged presence of GO may cause chronic toxicity in cells in case of rapid degradation of RSV and HAP. To address this issue, the PCL-PEG polymer composite were chosen to regulate the controlled release of these

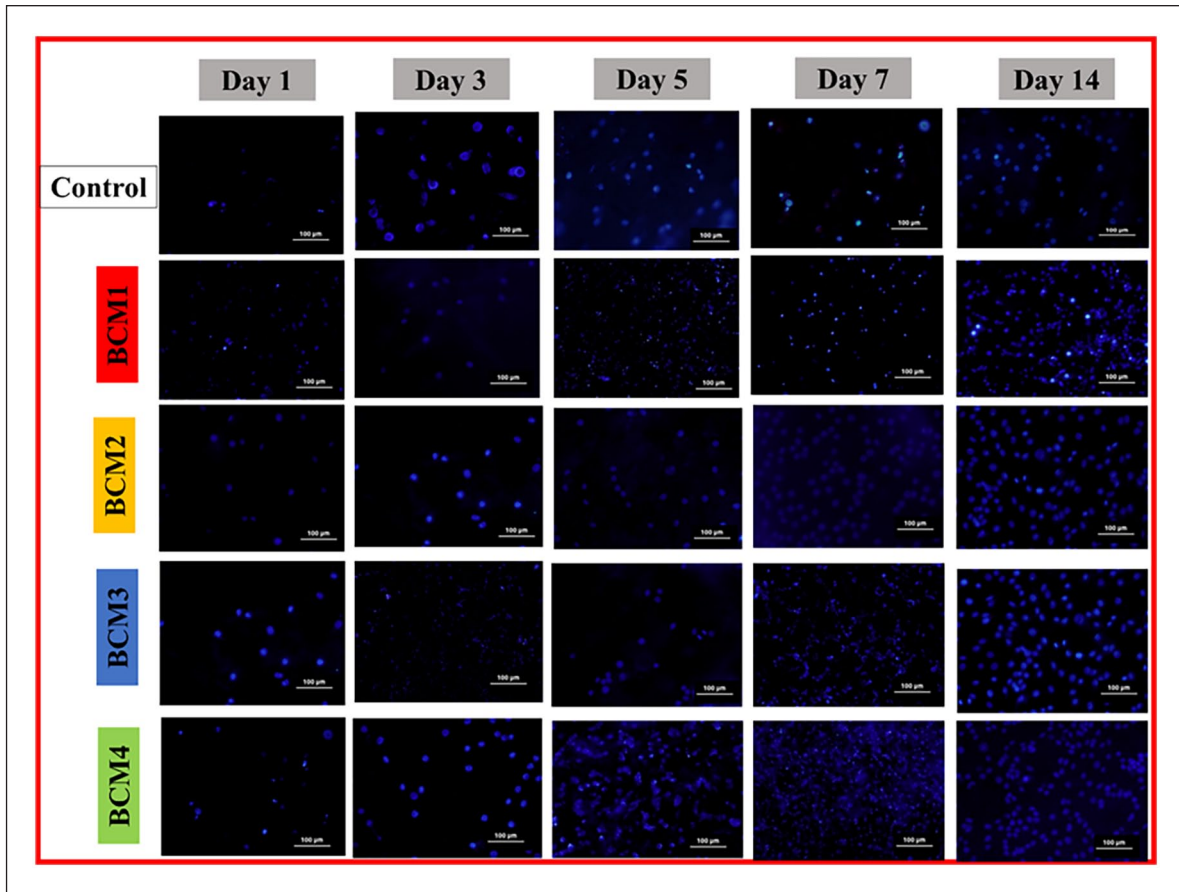


Figure 6. Fluorescence microscopy images of cells treated with various samples on days 1, 2, 3, 5, 7, and 14, with cells stained using DAPI following treatment.

materials. The electrospinning method was used to improve the release kinetics and to achieve slow degradation of the three materials.^{54–56} The PCL-PEG matrix utilized in current study capitalized on the advantageous properties of both polymers. PCL, is known for its biodegradability and mechanical stability, was chosen to provide necessary structural support and PEG was chosen to improve hydrophilicity, which is critical for facilitating cell adhesion and proliferation.⁵⁷ SEM analysis confirmed that loading RSV into the PCL-PEG matrix did not alter the composite's morphology (Figure 1). The nanofiber composite structures were consistent with those reported in previous studies^{58,59} confirming the reproducibility of the observed structures. The fiber diameter distribution varied across the samples due to differences in solution viscosity and the electrospinning process. For instance, PCL-PEG fibers exhibited a uniform distribution of fiber diameters, while the diameters of BCM samples containing GO and HAP show a slightly broader range. Among the samples, BCM4, which contains the highest doping of GO and HAP, exhibited the thinnest fibers, with average diameters of approximately 1386.055 ± 355.193 nm. This reduction in fiber diameter might be attributed to the influence of GO and

HAP on the electrospinning solution properties, specifically by altering its viscosity and electrical conductivity, which agrees with findings from recent studies.^{33,60} The fiber diameter distribution across samples was consistent with that of collagen fibrils in the ECM, which typically range between 50 and 500 nm.⁶¹ This similarity is crucial for mimicking the ECM structure in tissue engineering applications, where fiber dimensions comparable to those of natural collagen fibrils play a pivotal role in supporting cell attachment and proliferation. In terms of fiber diameters, the observations are consistent with recent literature. For example, studies on electrospun PCL and PCL-based composites often report fiber diameters in the range of 200–600 nm,^{62,63} which aligns with the range observed in the PCL-PEG and BCM samples. The inclusion of nanoparticles such as GO or HAP in electrospun fibers has also been shown to influence fiber diameter, often resulting in smaller fibers due to increased solution conductivity and a higher stretching force during electrospinning.^{64,65} Additionally, SEM images of biocomposite membranes incorporating GO and/or HAP revealed that these additives do not adversely affect the morphology of the composite. The structure remains intact and similar to

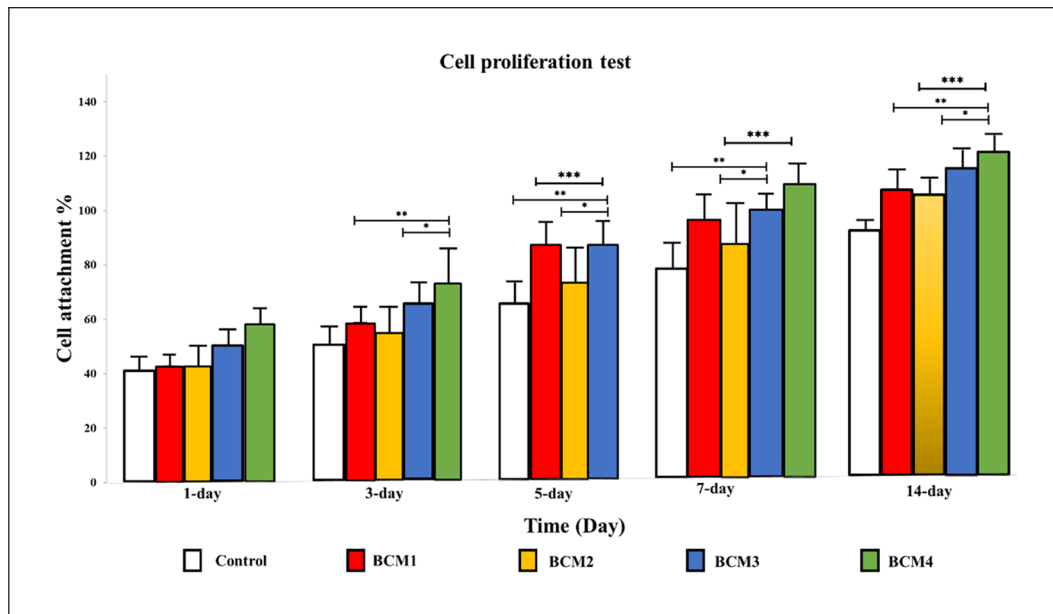


Figure 7. Percentage (%) of L929 cells attachment on the different samples. *, **, and *** indicate that statistical significance level was determined as $p < 0.05$.

that of the PCL-PEG and BCM1 composites, demonstrating that the incorporation of GO and/or HAP does not negatively impact the overall integrity of the composites. This finding is consistent with previous studies.^{66,67} Thus, RSV can be effectively loaded into the scaffolds while preserving their structural integrity.

Obtained results demonstrated that the mechanical properties of the modified membranes, including tensile strength, modulus, elongation at break, and toughness, were favorable, indicating that the scaffolds are robust enough for load-bearing bone defects (Figure 3 and Table 1). The incorporation of GO and HAP enhanced both the mechanical properties and biological activity, which are critical for scaffolds in BTE. These improvements are significant, as scaffolds must mimic the mechanical properties of natural bone to support physiological loads and promote cell attachment and proliferation.⁶⁸ Notably, the integration of GO into the PCL-PEG matrix not only improved the mechanical properties but also enhanced cell growth due to its high surface area and biocompatibility.⁶⁸ Obtained results showed that the BCM4 scaffold loaded with HAP exhibited the following optimal properties: the highest elongation at 9.8%, the greatest strength at 105.2 MPa, the best toughening effect at 3895 MPa, the best elongation performance at 8.4%, and the highest toughness value at 5.88 MJ/m³. These findings demonstrated the synergistic effect of combining GO, HAP, and RSV, which is consistent with previous studies.^{8,60} For example, in other studies, GO nanosheets containing Mg/Se- HAP co-substitution for wound healing applications were incorporated into PCL to be produced in nanofibrous scaffolds. The mechanical properties of the

nanofibrous scaffold were examined and it was shown that the fracture toughness increased from 0.66 ± 0.12 MJ/m³ to 3.10 ± 0.21 MJ/m³ at the lowest and highest GO, respectively, while the fracture strength increased from 0.81 ± 0.22 MPa to 4.4 ± 0.45 MPa.⁶⁹ In another study, mechanical results on PCL, HAP, GO nanocomposites showed that mechanical properties decreased when GO content was increased, while PCL regained its mechanical properties when HAP was added to the matrix.⁷⁰ Obtained results showed that the incorporation of GO, even at a low concentration, played a crucial role in promoting cellular adhesion to the RSV drug (Figures 6 and 7), leading to an enhanced degree of proliferation. Therefore, the inclusion of GO in the biocomposite construct had a positive impact on cellular adhesion and proliferation of the RSV drug, signifying its promising potential for beneficial applications in bone tissue engineering. The improvements observed in this study are consistent with previous research, which demonstrates that GO enhances scaffold performance by creating a more supportive environment for cellular activities.^{71,72} Similarly, it may be assumed that HAP, a mineral component resembling natural bone, boosts the bioactivity of the scaffold, fostering mineralization and better integration with surrounding bone tissue.⁵⁷ Previous studies demonstrated increased cell adhesion and proliferation over time, with HAP likely contributing to these effects due to its osteoconductive properties.^{73–76} Obtained results showed that the incorporation of GO and HAP into the substrate enhanced the pharmaceutical efficacy and tissue engineering applicability of the PCL-PEG polymeric material. These additions did not render the BCM structures cytotoxic. Furthermore, they improved

the chemical stability of PCL-PEG/RSV by imparting the bioactive properties of HAP and enhanced tissue engineering applicability by introducing the hydrophilic properties of GO.^{46,48,54} Therefore, the synergistic effects of PCL, PEG, GO, and HAP can result in a scaffold that effectively balances biological activity and mechanical properties.

The controlled and sustained release of RSV, as demonstrated by high R^2 for Korsmeyer–Peppas, Higuchi, and Baker models (Figures 4 and 5), is crucial for maintaining therapeutic levels over time and ensuring effective bone regeneration. The overall results of the release studies indicated the suitability of RSV-loaded composite conjugates as a means of providing sustained amounts of RSV. The initial therapeutic burst release of RSV indicates that by delivering a high concentration of the drug immediately, the tissue can help to immediately control or reduce the spread of disease. The sustained release phase of RSV was observed due to the remaining of active drug over time after the initial burst. The obtained results indicated that the overall treatment may lead to improved therapeutic outcomes as well as more effective. Overall, the initial burst release functions as a loading dose that effectively controls disease progression. Moreover, the sustained release phase further enhances therapeutic efficacy and outcomes.^{26,46,77} However, *in vitro* release kinetics might not fully capture the complexities of the *in vivo* environment. Factors such as polymer degradation, RSV interactions with biological fluids, and enzyme activity could impact the drug release profile in a physiological setting.^{78–80}

Several limitations of the study should be considered in the interpretation of these results. These results were obtained under controlled conditions and may not fully replicate the *in vivo* environment. Further research, including *in vivo* studies, is necessary to assess how these scaffolds interact with live tissue and support bone regeneration in a more complex biological context. Another limitation of the current study is the use of DAPI dye, which primarily stains the nuclear structure. While methods like F-actin staining are commonly employed to observe the longitudinal shape of the cell, the nuclear morphology observed with DAPI can still provide valuable insights into cell shape. Many studies have demonstrated the relationship between nuclear morphology and overall cell shape.^{81–83} Additionally, the long-term stability and degradation of the biocomposite membranes were not evaluated, which are critical for understanding the membranes' performance over time. Moreover, while the release kinetics models offer insights into drug release, they do not account for variability due to physiological conditions such as pH changes, enzyme activity, and interactions with biological fluids.

Conclusion

The novelty of this study lies in its multifunctional biocomposite membrane (BCM4), which incorporates a well-optimized combination of PCL-PEG polymers with GO,

HAP, and RSV, leading to an advanced scaffold with superior mechanical properties, morphological integrity, and sustained drug delivery potential. These scaffolds represent a significant improvement over existing models by offering both enhanced mechanical strength and sustained drug release, making them potentially ideal candidates for bone tissue engineering applications. In summary, RSV-loaded PCL-PEG/GO/HAP biocomposite membranes hold significant promise for bone tissue engineering since they improve mechanical and biological properties while providing a controlled and sustained drug release profile. This composite system can potentially enhance osteogenic differentiation, mechanical properties, and bioactivity, thereby improving the efficacy of scaffolds used for bone regeneration. Continued research and development are still crucial for refining these scaffolds and enhancing their clinical outcomes in bone repair and regeneration. Future research should address the limitations by conducting *in vivo* preclinical and clinical trials to evaluate the performance of RSV-loaded biocomposite membranes under real physiological conditions. Further optimization of scaffold designs and advanced imaging techniques could enhance the clinical applicability of these materials.

Acknowledgements

The authors would like to thank Fatih Sultan Mehmet Vakıf University Technology Transfer Office and Biomedical Department Biomaterials BİORGİNE Laboratory for supporting this study.

Author contributions

Betül Meryem Arpacay: Conceptualization, Methodology, Investigation, Formal analysis, Writing – original draft, Visualization. Fatih Ciftci: Conceptualization, Methodology, Investigation, Formal analysis, Writing – original draft, Visualization and Supervisor. Ali Can Özarslan: Conceptualization, Methodology, Formal analysis, Writing – review and editing. Mustafa Unal: Conceptualization, Methodology, Writing – original draft, Writing – review and editing. Mine Kucak: Conceptualization, Methodology, Writing – review and editing. Aslihan Yelkenci: Conceptualization, Methodology, Writing – review and editing.

Data and code availability

The authors confirm that the data supporting the findings of this study are available within the article. Raw data that support the findings of this study are available from the corresponding author, upon reasonable request.

Declaration of conflicting interests

The author(s) declared no potential conflicts of interest with respect to the research, authorship, and/or publication of this article.

Funding

The author(s) received no financial support for the research, authorship, and/or publication of this article.


Ethical approval

Not applicable.

ORCID iDs


Betül Meryem Arpacay  <https://orcid.org/0009-0004-6229-2157>

Fatih Ciftci  <https://orcid.org/0000-0002-3062-2404>

Ali Can Özarslan  <https://orcid.org/0000-0002-4864-0598>

Mustafa Unal  <https://orcid.org/0000-0002-9518-8952>

Mine Kucak  <https://orcid.org/0000-0003-3991-4953>

Aslihan Yelkenci  <https://orcid.org/0000-0001-6076-1715>

References

- Salari N, Ghasemi H, Mohammadi L, et al. The global prevalence of osteoporosis in the world: a comprehensive systematic review and meta-analysis. *J Orthop Surg Res* 2021; 16: 609.
- Khan Y, Yaszemski MJ, Mikos AG, et al. Tissue engineering of bone: material and matrix considerations. *J Bone Joint Surg* 2008; 90: 36–42.
- Betz RR. Limitations of autograft and allograft: new synthetic solutions. *Orthopedics* 2002; 25: (5 Suppl): s561–s570.
- Kalsi S, Singh J, Sehgal SS, et al. Biomaterials for tissue engineered bone Scaffolds: a review. *Mater Today Proc* 2021; 81: 888–893.
- Ciftci F and Özarslan AC. Preparation of PLGA-PEG/hydroxyapatite composites via simple methodology of film formation and assessment of their structural, thermal, and biological features. *J Turk Chem Soc Sect A Chem* 2023; 10: 1123–1132.
- Ciftci F and Özarslan AC. Comprehensive assessment of PLGA/nHAp combined with Hemp oil bionanocomposites: revealing the in vitro behavior and features. *Nano Struct Nano Objects* 2024; 38: 101152.
- Wang W, Junior JRP, Nalesso PRL, et al. Engineered 3D printed poly(ϵ -caprolactone)/graphene scaffolds for bone tissue engineering. *Mater Sci Eng C* 2019; 100: 759–770.
- Loyo C, Cordoba A, Palza H, et al. Effect of gelatin coating and GO incorporation on the properties and degradability of electrospun PCL scaffolds for bone tissue regeneration. *Polymers* 2024; 16: 129.
- Suganya S, Venugopal J, Ramakrishna S, et al. Herbally derived polymeric nanofibrous scaffolds for bone tissue regeneration. *J Appl Polym Sci* 2014; 131(3): 39835.
- Prasadh S, Suresh S and Wong R. Osteogenic potential of graphene in bone tissue engineering scaffolds. *Materials* 2018; 11(8): 1430.
- Feng W, Wang J, Li B, et al. Graphene oxide leads to mitochondrial-dependent apoptosis by activating ROS-p53-mPTP pathway in intestinal cells. *Int J Biochem Cell Biol* 2022; 146: 106206.
- Dutta T, Sarkar R, Pakhira B, et al. ROS generation by reduced graphene oxide (rGO) induced by visible light showing antibacterial activity: comparison with graphene oxide (GO). *RSC Adv* 2015; 5: 80192–80195.
- Luo Y, Shen H, Fang Y, et al. Enhanced proliferation and osteogenic differentiation of mesenchymal stem cells on graphene oxide-incorporated electrospun poly(lactic-co-glycolic acid) nanofibrous mats. *ACS Appl Mater Interf* 2015; 7: 6331–6339.
- Dalgic AD, Alshemary AZ, Tezcaner A, et al. Silicate-doped nano-hydroxyapatite/graphene oxide composite reinforced fibrous scaffolds for bone tissue engineering. *J Biomater Appl* 2018; 32: 1392–1405.
- Lebre F, Sridharan R, Sawkins MJ, et al. The shape and size of hydroxyapatite particles dictate inflammatory responses following implantation. *Scient Rep* 2017; 7: 2922.
- Mestres G, Espanol M, Xia W, et al. Inflammatory response to nano- and microstructured hydroxyapatite. *PLoS ONE* 2015; 10: e0120381.
- Jang JE, Kim HM, Kim H, et al. Inflammatory responses to hydroxyapatite/poly(lactic-co-glycolic acid) scaffolds with variation of compositions. *Polymer (Korea)* 2014; 38: 156–163.
- Kolanthai E, Sindu PA, Khajuria DK, et al. Graphene oxide—a tool for the preparation of chemically crosslinking free Alginate-Chitosan-Collagen scaffolds for bone tissue engineering. *ACS Appl Mater Interf* 2018; 10: 12441–12452.
- Dong L, Wang SJ, Zhao XR, et al. 3D-printed poly(ϵ -caprolactone) scaffold integrated with cell-laden chitosan hydrogels for bone tissue engineering. *Scient Rep* 2017; 7: 121131.
- Diban N, Sánchez-González S, Lázaro-Díez M, et al. Facile fabrication of poly(ϵ -caprolactone)/graphene oxide membranes for bioreactors in tissue engineering. *J Membr Sci* 2017; 540: 219–228.
- Du Y, Liu H, Yang Q, et al. Selective laser sintering scaffold with hierarchical architecture and gradient composition for osteochondral repair in rabbits. *Biomaterials* 2017; 137: 37–48.
- Moon DK, Kim BG, Lee AR, et al. Resveratrol can enhance osteogenic differentiation and mitochondrial biogenesis from human periosteum-derived mesenchymal stem cells. *J Orthop Surg Res* 2020; 15: 203.
- Wajima CS, Pitol-Palin L, de Souza Batista FR, et al. Morphological and biomechanical characterization of long bones and peri-implant bone repair in type 2 diabetic rats treated with resveratrol. *Scient Rep* 2024; 14: 2860.
- Ozturk S, Cuneyit I, Altuntas F, et al. Resveratrol prevents ovariectomy-induced bone quality deterioration by improving the microarchitectural and biophysicochemical properties of bone. *J Bone Min Metab* 2023; 41: 443–456.
- Bo S, Gambino R, Ponzo V, et al. Effects of resveratrol on bone health in type 2 diabetic patients. A double-blind randomized-controlled trial. *Nutr Diab* 2018; 8: 51.
- Ciftci F. Release kinetics modelling and in vivo-vitro, shelf-life study of resveratrol added composite transdermal scaffolds. *Int J Biol Macromol* 2023; 235: 123769.
- Ikeda E, Tanaka D, Glogauer M, et al. Healing effects of monomer and dimer resveratrol in a mouse periodontitis model. *BMC Oral Health* 2022; 22: 460.
- Khalid S, Afzal N, Khan JA, et al. Antioxidant resveratrol protects against copper oxide nanoparticle toxicity in vivo. *Naunyn Schmiedebergs Arch Pharmacol* 2018; 391: 1053–1062.
- Lee SH and Lee YJ. Synergistic anticancer activity of resveratrol in combination with docetaxel in prostate carcinoma cells. *Nutr Res Pract* 2021; 15: 12–25.

30. Özdemir DG, Evcimen Duygulu N, Özarslan AC, et al. Fabrication and characterization of graphene oxide/fucoidan/chitosan reinforced poly(vinyl alcohol) nanocomposites. *J Mol Struct* 2024; 1301: 137330.
31. Ciftci F and Özarslan AC. Fabrication of polycaprolactone-chitosan/curcumin polymer composite fibers and evaluation of their in vitro release kinetic behavior and antibacterial-antifungal activity. *J SolGel Sci Technol* 2023; 109: 192–203.
32. Ciftci F, Özarslan AC and Evcimen Duygulu N. Production and comprehensive characterization of PVA/chitosan transdermal composite mats loaded with bioactive curcumin; evaluation of its release kinetics, antioxidant, antimicrobial, and biocompatibility features. *J Appl Polym Sci* 2024; 141: e55874.
33. Ozder MN, Ciftci F, Rencuzogullari O, et al. In situ synthesis and cell line studies of nano-hydroxyapatite/graphene oxide composite materials for bone support applications. *Ceram Int* 2023; 49: 14791–14803.
34. Khenoussi N, Hekmati AH, Drean E, et al. Study of rheological behaviour of polymer solution used for electrospinning proces. In *Proceedings of the fiber society 2009 spring conference*, Shanghai, China, 27–29 May 2009, pp. 474–475.
35. Jayamani E, Loong TG and Bakri MKB. Comparative study of Fourier transform infrared spectroscopy (FTIR) analysis of natural fibres treated with chemical, physical and biological methods. *Polym Bull* 2020; 77: 1605–1629.
36. Saini BS and Kaur R. *Handbook of modern coating technologies: advanced characterization methods*. Amsterdam, The Netherlands: Elsevier, 2021, pp. 85–141.
37. Raj SS, Michailovich KA, Subramanian K, et al. Philosophy of selecting ASTM standards for mechanical characterization of polymers and polymer composites. *Mater Plast* 2021; 58: 247–256.
38. Oh JY, Yang G, Choi E, et al. Mesoporous silica nanoparticle-supported nanocarriers with enhanced drug loading, encapsulation stability, and targeting efficiency. *Biomater Sci* 2022; 10: 1448–1455.
39. Górska A, Krupa A, Majda D, et al. Poly(vinyl alcohol) cryogel membranes loaded with resveratrol as potential active wound dressings. *AAPS PharmSciTech* 2021; 22(3): 109.
40. Poonia N, Lather V, Kaur B, et al. Optimization and development of methotrexate- and resveratrol-loaded nanoemulsion formulation using box-behnken design for rheumatoid arthritis. *Assay Drug Develop Technol* 2020; 18: 356–368.
41. Isailović BD, Kostić IT, Zvonar A, et al. Encapsulation of natural antioxidant resveratrol in liposomes. In: *CEFood 2012 - Proceedings of 6th Central European congress on food*, Serbia, Africa, 23–26 May 2012, pp. 1046–1051.
42. Ciftci F, Duygulu N, Yilmazer Y, et al. Antibacterial and cellular behavior of PLA-based bacitracin and zataria multiflora nanofibers produced by electrospinning method. *Int J Polym Mater Polym Biomater* 2023; 72: 319–334.
43. Pinar E, Sahin A, Unal S, et al. The effect of polycaprolactone/graphene oxide electrospun scaffolds on the neurogenic behavior of adipose stem cells. *Eur Polym J* 2022; 165: 111000.
44. Rajitha K and Mohana KN. Application of modified graphene oxide—polycaprolactone nanocomposite coating for corrosion control of mild steel in saline medium. *Mater Chem Phys* 2020; 241: 122050.
45. Karimi-Soflou R, Mohseni-Vadeghani E and Karkhaneh A. Controlled release of resveratrol from a composite nanofibrous scaffold: effect of resveratrol on antioxidant activity and osteogenic differentiation. *J Biomed Mater Res A* 2022; 110: 21–30.
46. Li L, Yu M, Li Y, et al. Synergistic anti-inflammatory and osteogenic n-HA/resveratrol/chitosan composite microspheres for osteoporotic bone regeneration. *Bioact Mater* 2021; 6: 1255–1266.
47. Karakucuk A and Tort S. Preparation, characterization and antimicrobial activity evaluation of electrospun PCL nanofiber composites of resveratrol nanocrystals. *Pharmac Develop Technol* 2020; 25: 1216–1225.
48. Gong X, Wang Y, Yao K, et al. Supercapacitors based on resveratrol/reduced graphene oxide composites. *ACS Appl Nano Mater* 2023; 6: 4162–4169.
49. de Nadai Dias FJ, de Andrade Pinto SA, Rodrigues dos Santos A, et al. Resveratrol-loaded polycaprolactone scaffolds obtained by rotary jet spinning. *Int J Polym Anal Charact* 2022; 27: 289–301.
50. Özarslan AC and Çiftçi F. A comparative study of release kinetics behavior models and shelf life assessment of bacitracin zinc-loaded PLA composites. *Konya J Eng Sci* 2023; 11: 1006–1015.
51. Xu Y, Kim CS, Saylor DM, et al. Polymer degradation and drug delivery in PLGA-based drug–polymer applications: a review of experiments and theories. *J Biomed Mater Res B Appl Biomater* 2017; 105: 1692–1716.
52. Colino CI, Lanao JM and Gutierrez-Millan C. Targeting of hepatic macrophages by therapeutic nanoparticles. *Front Immunol* 2020; 11: 218.
53. Hasan A, Waibhaw G, Tiwari S, et al. Fabrication and characterization of chitosan, polyvinylpyrrolidone, and cellulose nanowhiskers nanocomposite films for wound healing drug delivery application. *J Biomed Mater Res A* 2017; 105: 2391–2404.
54. Ekambaram R and Dharmalingam S. Design and development of biomimetic electrospun sulphonated polyether ether ketone nanofibrous scaffold for bone tissue regeneration applications: in vitro and in vivo study. *J Biomater Sci Polym Ed* 2022; 33: 947–975.
55. Tao ZS, Zhou WS, Yang M, et al. Resveratrol reverses the negative effect of alcohol on hydroxyapatite-coated implant osseointegration in senile female rats. *Zeitschrift fur Gerontol Geriatr* 2020; 53: 538–545.
56. Gupta A, Kumar Mehta S, Qayoom I, et al. Bio-functionalization with *Cissus quadrangularis* phyto-bio-actives accentuates nano-hydroxyapatite based ceramic nano-cement for neo-bone formation in critical sized bone defect. *Int J Pharmac* 2023; 642: 123110.
57. Bose S, Sarkar N and Banerjee D. Effects of PCL, PEG and PLGA polymers on curcumin release from calcium phosphate matrix for in vitro and in vivo bone regeneration. *Mater Today Chem* 2018; 8: 110–120.
58. Zhang Z, Ji Y, Hu N, et al. Ferroptosis-induced anticancer effect of resveratrol with a biomimetic nano-delivery system in colorectal cancer treatment. *Asian J Pharmac* 2022; 17: 751–766.

59. Sanna V, Siddiqui IA, Sechi M, et al. Resveratrol-loaded nanoparticles based on poly(epsilon-caprolactone) and poly(D,L-lactic-co-glycolic acid)-poly(ethylene glycol) blend for prostate cancer treatment. *Mol Pharmacol* 2013; 10: 3871–3881.
60. Nasari M, Poursharifi N, Fakhrali A, et al. Fabrication of novel PCL/PGS fibrous scaffold containing HA and GO through simultaneous electrospinning-electrospray technique. *Int J Polym Mater Polym Biomater* 2023; 72: 1529–1545.
61. Aumailley M and Gayraud B. Structure and biological activity of the extracellular matrix. *J Mol Med* 1998; 76: 253–265.
62. Sreerekha PR, Menon D, Nair SV, et al. Fabrication of fibrin based electrospun multiscale composite scaffold for tissue engineering applications. *J Biomed Nanotechnol* 2013; 9: 790–800.
63. Kamaruzaman NA, Yusoff ARM, Malek NANN, et al. Fabrication, characterization and degradation of electrospun poly(epsilon-caprolactone) infused with selenium nanoparticles. *Mal J Fund Appl Sci* 2021; 17: 295–305.
64. Drakopoulos SX, Yang J, Vryonis O, et al. Flexible polymer-based nanodielectrics reinforced with electrospun composite nanofibers for capacitive energy storage. *ACS Appl Polym Mater* 2022; 4: 8203–8215.
65. Han C, Cai N, Chan V, et al. Enhanced drug delivery, mechanical properties and antimicrobial activities in poly(lactic acid) nanofiber with mesoporous Fe₃O₄-COOH nanoparticles. *Coll Surf Physicochem Eng Aspects* 2018; 559: 104–114.
66. Guo X, Mei J and Zhang C. Development of drug dual-carriers delivery system with mitochondria-targeted and pH/heat responsive capacity for synergistic photothermal-chemotherapy of ovarian cancer. *Int J Nanomed* 2020; 15: 301–313.
67. Chakraborty S, Vimalnath KV, Rajeswari A, et al. Preparation, evaluation, and first clinical use of ¹⁷⁷Lu-labeled hydroxyapatite (HA) particles in the treatment of rheumatoid arthritis: utility of cold kits for convenient dose formulation at hospital radiopharmacy. *J Label Comp Radiopharmac* 2014; 57: 453–462.
68. Shuai C, Peng B, Feng P, et al. In situ synthesis of hydroxyapatite nanorods on graphene oxide nanosheets and their reinforcement in biopolymer scaffold. *J Adv Res* 2022; 35: 13–24.
69. Ahmed MK, Mansour SF, Al-Wafi R, et al. Composition and design of nanofibrous scaffolds of Mg/Se-hydroxyapatite/graphene oxide @ epsilon-polycaprolactone for wound healing applications. *J Mater Res Technol* 2020; 9(4): 7472–7485.
70. Medeiros GS, Muñoz PAR, de Oliveira CFP, et al. Polymer nanocomposites based on poly(epsilon-caprolactone), hydroxyapatite and graphene oxide. *J Polym Environ* 2020; 28: 331–342.
71. Cheng J, Liu H, Zhao B, et al. MC3T3-E1 preosteoblast cell-mediated mineralization of hydroxyapatite by poly-dopamine-functionalized graphene oxide. *J Bioact Compat Polym* 2015; 30: 289–301.
72. Keny Chaudhuri PK, Loh KP, et al. Selective accelerated proliferation of malignant breast cancer cells on planar graphene oxide films. *ACS Nano* 2016; 10: 3424–3434.
73. Nareswari TL, Juniatik M, Aminatun A, et al. A facile technique for overcoming seeding barriers of hydrophobic polycaprolactone/hydroxyapatite-based nanofibers for bone tissue engineering. *J Appl Pharmac Sci* 2023; 13: 49–60.
74. Depan D, Pesacreta TC and Misra RDK. The synergistic effect of a hybrid graphene oxide-chitosan system and biomimetic mineralization on osteoblast functions. *Biomater Sci* 2014; 2: 264–274.
75. Frohbergh ME, Katsman A, Botta GP, et al. Electrospun hydroxyapatite-containing chitosan nanofibers crosslinked with genipin for bone tissue engineering. *Biomaterials* 2012; 33: 9167–9178.
76. Li M, Xiong P, Yan F, et al. An overview of graphene-based hydroxyapatite composites for orthopedic applications. *Bioact Mater* 2018; 3: 1–18.
77. Zemljič LF, Maver U, Glaser TK, et al. Electrospun composite nanofibrous materials based on (Poly)-phenol-polysaccharide formulations for potential wound treatment. *Materials* 2020; 13: 2631.
78. Asikainen S and Seppälä J. Photo-crosslinked anhydride-modified polyester and -ethers for pH-sensitive drug release. *Eur J Pharmac Biopharmac* 2020; 150: 33–42.
79. Li J, Li L, Wu T, et al. An injectable thermosensitive hydrogel containing resveratrol and dexamethasone-loaded carbonated hydroxyapatite microspheres for the regeneration of osteoporotic bone defects. *Small Methods* 2024; 8: e2300843.
80. Li Y, Dnmark S, Edlund U, et al. Resveratrol-conjugated poly-epsilon-caprolactone facilitates in vitro mineralization and in vivo bone regeneration. *Acta Biomater* 2011; 7: 751–758.
81. Devulapally A, Parekh V, Pazhayidam George C, et al. On the variability in cell and nucleus shapes. *Cells Tissues Organs* 2022; 213: 96–107.
82. Lecuit T and Lenne PF. Cell surface mechanics and the control of cell shape, tissue patterns and morphogenesis. *Nat Rev Mol Cell Biol* 2007; 8: 633–644.
83. Paluch E and Heisenberg CP. Biology and physics of cell shape changes in development. *Curr Biol* 2009; 19: R790–R799.